Electronic Supplementary Material (ESI)

"Gas-phase aluminium acetylacetonate decomposition: Revision of the current mechanism by VUV synchrotron radiation"

Sebastian Grimm*[a,e], Seung-Jin Baik[b,e], Patrick Hemberger[c], Andras Bodi[c], Andreas Kempf[b,e], Tina Kasper[d,e] and Burak Atakan[a,e]

[a] *University of Duisburg-Essen, Institute of Combustion and Gas Dynamics, Chair of Thermodynamics, Duisburg 47057, Germany.*

[b] *University of Duisburg-Essen, Institute of Combustion and Gas Dynamics, Chair of Fluid dynamics, Duisburg 47057, Germany.*

[c] *Laboratory for Synchrotron Radiation and Femtochemistry, Paul Scherrer Institute, CH-5232 Villigen-PSI, Switzerland.*

[d] *University of Duisburg-Essen, Institute of Combustion and Gas Dynamics, Chair of Mass spectrometry of reactive fluids, Duisburg 47057, Germany.*

[e] *Center for NanoIntegration Duisburg-Essen (CENIDE), Duisburg 47057, Germany.*

S1 Numerical simulation of the microreactor

S 1.1 General equations and assumptions

The Navier-Stokes equations contain mass continuity and momentum conservation written as

$$\frac{\partial \rho}{\partial t} + \frac{\partial}{\partial x_i}(\rho u_i) = 0 \quad \textbf{(E1)}$$

$$\frac{\partial}{\partial t}(\rho u_i) + \frac{\partial}{\partial x_j}(\rho u_i u_j) = -\frac{\partial p}{\partial x_j}\left[\mu\left(\frac{\partial u_i}{\partial x_j} + \frac{\partial u_j}{\partial x_i} - \frac{2}{3}\delta_{ij}\frac{u_l}{\partial x_l}\right)\right] + \frac{\partial}{\partial x_k}\left(-\rho\overline{u_i' u_j'}\right) \quad \textbf{(E2)}$$

where μ is the dynamic viscosity. In the present work, the Knudsen number (*Kn*) is used as key parameter to determine the rarefaction level of the investigation region. The Reynolds and Mach number define the local *Kn* as follows,

$$Kn \equiv \frac{\lambda}{L} = \sqrt{\frac{\gamma\pi}{2}}\frac{M}{Re} \quad \textbf{(E3)}$$

$$Re = \frac{\rho U d}{\mu} \quad \textbf{(E4).}$$

Generally, depending on the value of *Kn*, the flow region can be divided into a continuous flow region (*Kn* < 0.01), a slip flow region (0.01 < *Kn* < 0.1), a transition flow region (0.1 < *Kn* < 10), and a free-molecular flow region (Kn > 10). Detailed transition of flow regimes based on the Knudsen number can be found elsewhere.[1]

By applying slip boundary condition, a simple approximation for slip fluid velocity at the wall is

$$V_{slip} = l_s \frac{\partial V}{\partial n}\bigg|_{at\ wall} \quad \textbf{(E5)}$$

, where *n* denotes the normal vector to the wall, and l_s is the slip length. The main difficulty to define the slip velocity comes from the treatment of the slip length. In the present work, the slip length l_s is calculated according to Morris et al.[2]:

$$l_s = \alpha L \cdot Kn \quad \textbf{(E6).}$$

The model constant α is suggested as 1.15 in their work. The heated length (10 mm) in the reactor is consequently used as the characteristic length *L*.

S 1.2. Computational domain and numerical setup

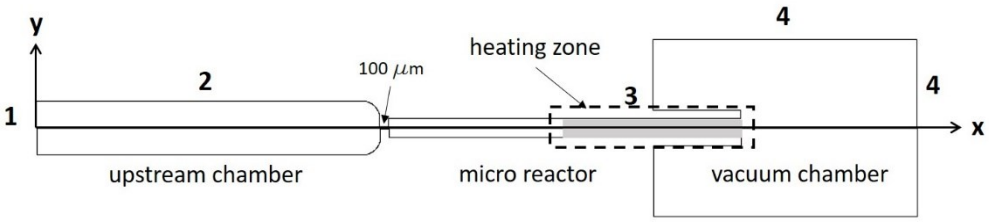

Fig. S 1 Two-dimensional axisymmetric geometry for the present simulation.

The computational domain is set up as axisymmetric two-dimensional geometry as shown in **Fig. S 1** with detailed boundary conditions as shown in **Tab. S 1**.

Tab. S 1 Boundary conditions for the domain in **Fig. S2**

Nr.	Boundary type	Pressure mbar	Temperature K
1	Inlet	550, 1600	293.15
2	No-slip wall	-	405.15
3	Slip wall	-	423.15 - 1273.15
4	Outlet	6×10^{-5}	-
5	Symmetric	-	-

In the present work, a cell size of 10 µm is used for the complete computational domain, in order to assure accurate results, while keeping the computational costs at a minimum. Applying this grid size gives us more than 10 nodes in radial direction to resolve the flow field of a tiny pinhole (100 µm) of the connection between evaporator (see **Fig. S1 Nr.2**) and reactor (see **Fig. S1 Nr.3**). To test the influence of a further refinement of the mesh size on the simulation results, we halved the cell size. There is no significant difference of the calculated flow field properties, as demonstrated in **Fig. S 2**. Thus, we conclude, that the cell size of 10 µm is sufficient to resolve the present computational domain at the conditions evaluated in this study.

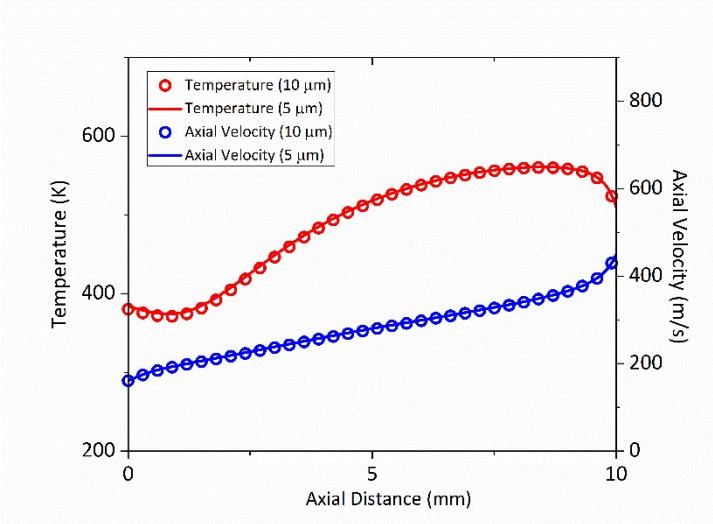

Fig. S 2 Axial profiles of the temperature and axial velocity for an outer surface temperature of 623 K at two grid sizes, 5µm and 10 µm.

S 1.3 Flow regime characteristics in the heated zone

Fig. S 3 shows the axial profiles of *Kn* in the heated zone of the reactor at wall temperatures of 553.15, 673.15 and 833.15 K. If the outer surface temperature is increased, the flow in the heating zone has a higher *Kn*. Since the range of *Kn* at the experimental outer surface temperatures of 348-1273 K is 0.005 ≤ *Kn* ≤ 0.02, we can assume that the flow in microreactor is located in the slip flow region.

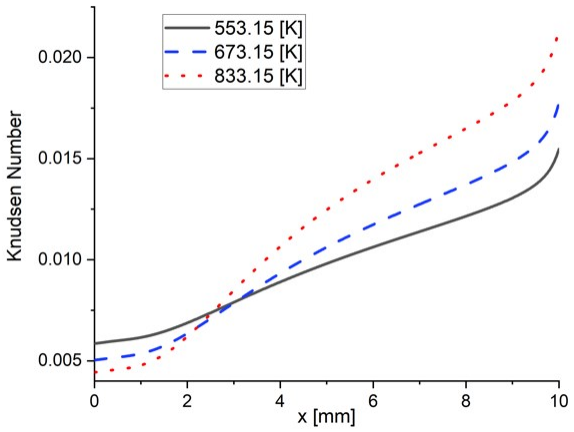

Fig. S 3 Axial profile of the local Knudsen number for various experimental surface temperatures.

S 1.4 Validation of the simulation

To validate the feasibility of the present simulation method, additional simulations were performed with the same conditions that were used for the simulation of a microreactor by Weddle et al.[3] A detailed description of the geometry and operating parameters can be found elsewhere.[3] Our simulation reproduced Weddle's conditions fairly well and shows a good agreement for important flow properties, as temperature and axial velocity, as shown in **Fig S4**. The deviations at the outlet section of the reactor (>30 mm) can be explained by the simulation domain used in both studies. Our domain does include the downstream vacuum chamber (see **4** in **Fig. S1**), in which the flow is expanded, whereas the reference test case does only consider the microreactor as simulation domain.

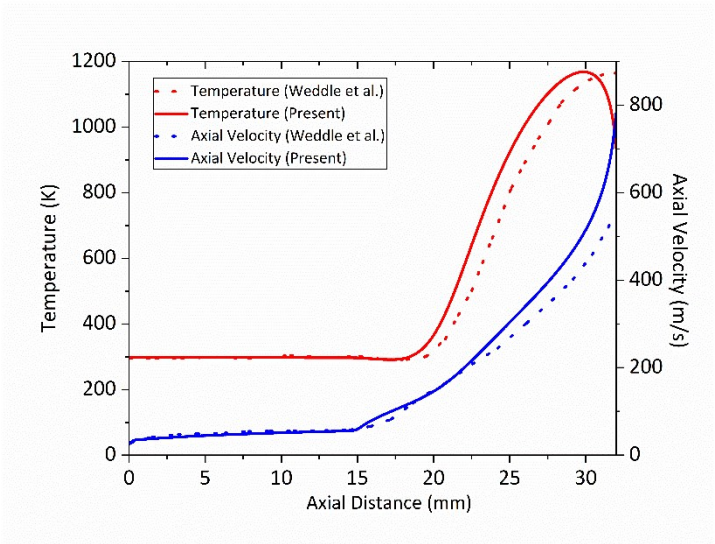

Fig. S 4 Axial centerline profiles of temperature (red) and axial velocity (blue) for a wall temperature of 1500 K and 1700 K. Data from Weddle et al.: dotted; our simulation: lines.[3]

S 1.5 Effect of wall reactions

Even though the residence time in the reaction (heating) zone is significantly smaller than in typical flow reactors, it is necessary to check whether surface reactions may dominate the mechanism under the experimental conditions. Guan et al.[4] tried to explain the influence of wall reactions by a comparison between the residence time and the characteristic time for radial diffusion expressed as $\tau_{diff} = r^2/D$. We also used this approach for our conditions, where *r* as the radius of the SiC microreactor and *D* is denoted as the diffusion coefficient of aluminium acetylacetonate in argon. Since, to our knowledge, there is no available data in the literature for the diffusion coefficient (aluminum acetylacetonate in argon), we approximate the diffusion coefficient with a correlation equation.[5] This correlation equation estimates the binary diffusion coefficient with empirical constants (so-called atomic diffusion volumes) found from experimental data. However, since the original equation does not contain the metal component, we adjusted the equation constants by the previous observation from Siddiqi et al.[6] (aluminium acetylacetonate in nitrogen).

Figure S 5 displays the residence time in the reaction zone is much smaller than the diffusion time scales except at wall temperatures higher than 1200 K. Therefore, we can assume that the surface reaction at

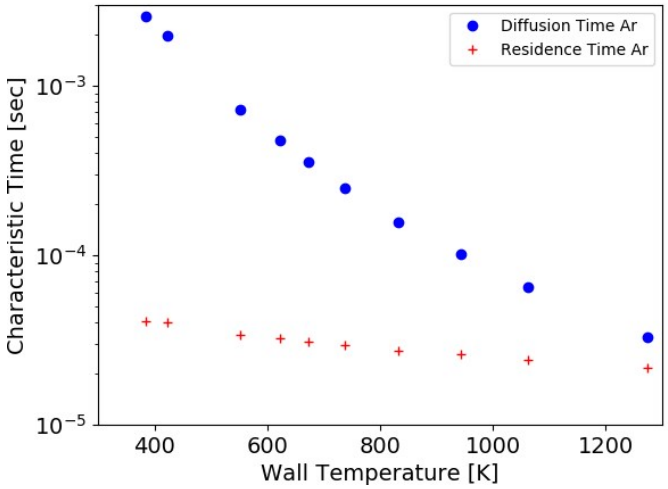

Fig. S 5 Comparison of residence and diffusion time for $Al(C_5H_7O_2)_3$.

the wall is rather small in the present temperature range.

S2 Temperature-dependent gas expansion factor

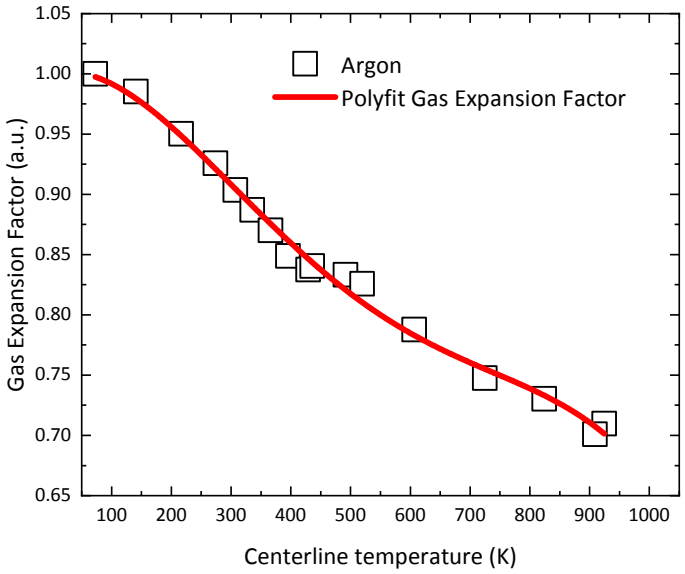

Fig. S 6: Gas expansion factor as a function of calculated centreline temperature according to the numerical simulation.

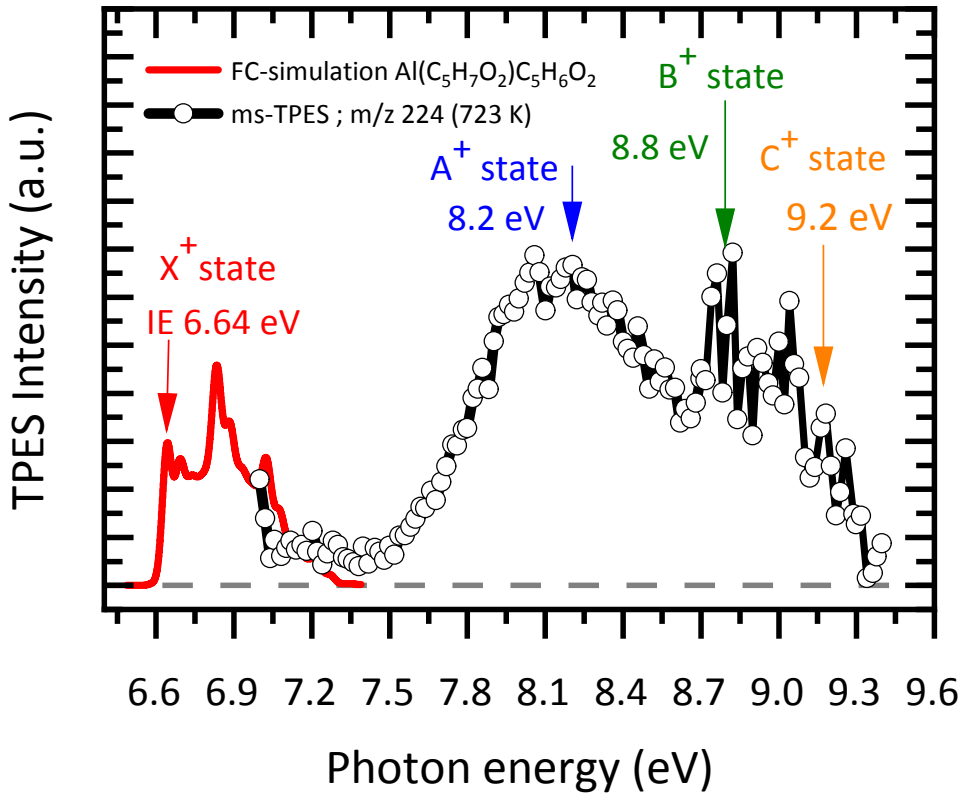

Fig. S 7 Assignment of the ms-TPES at *m/z* 224 (dotted black curve) to $Al(C_5H_7O_2)C_5H_6O_2$, based on computed IEs from Franck-Condon simulations of $Al(C_5H_7O_2)C_5H_6O_2$ (red curve). Blue, green and yellow notations belong to calculated excited states of the molecule.

S3 Assignment of *m/z* 224, $Al(C_5H_7O_2)C_5H_6O_2$

S4 Species assignments of further decomposition products

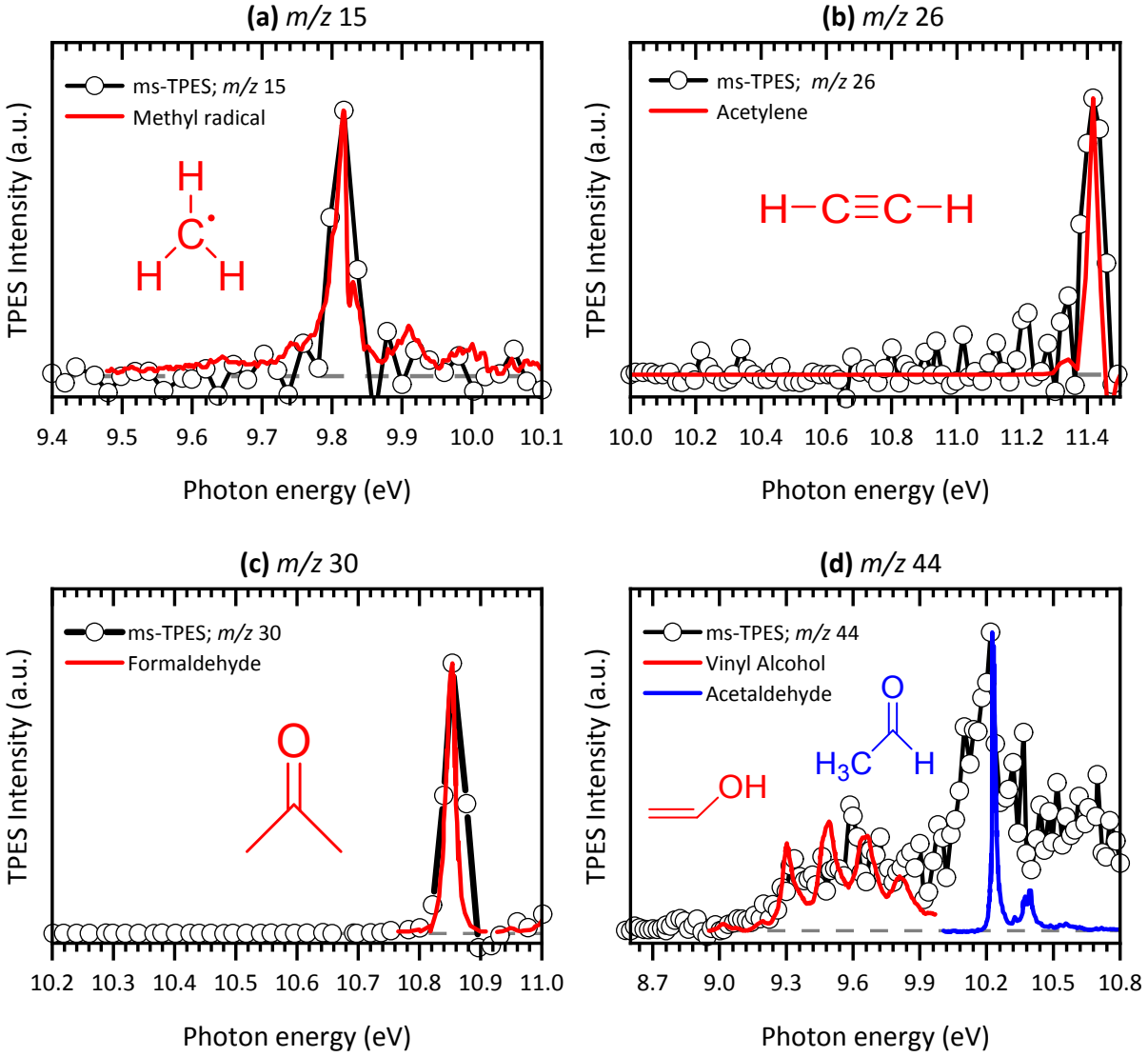

Fig. S 8 Representative examples of product species identification and assignment for C-C_3 hydrocarbons and oxygenated species in the pyrolysis of $Al(C_5H_7O_2)_3$ using TPE-spectra (black lines, dot symbol); Literature reference spectra (red, blue) are as follows: **(a)** *m/z* 15 (CH_3)[7] **(b)** *m/z* 26 (C_2H_2)[8] **(c)** *m/z* 30 (CH_2O)[9] and **(d)** *m/z* 44 (C_2H_3OH)[10] and (C_2H_4O)[11].

At 9.82 eV, a clear peak in the TPES of *m/z* 15 emerges, which corresponds to the published ionization potential of the methyl radical (IE = 9.84 eV[7]) (see **Fig. S 8 (a)**). The spectrum in **Fig. S 8 (b)** is consistent with the reported spectrum of acetylene (C_2H_2)[8] and the experimental data in **(c)** is in line with the spectrum obtained by others for the photoionization of formaldehyde (CH_2O) at IE = 8.71 eV.[9] Strong evidence of a mixture of vinyl alcohol[10] and acetaldehyde[11] was found at the *m/z* 44 channel by comparing the TPE-spectrum to reference spectra in **Fig. S 8 (d)**.

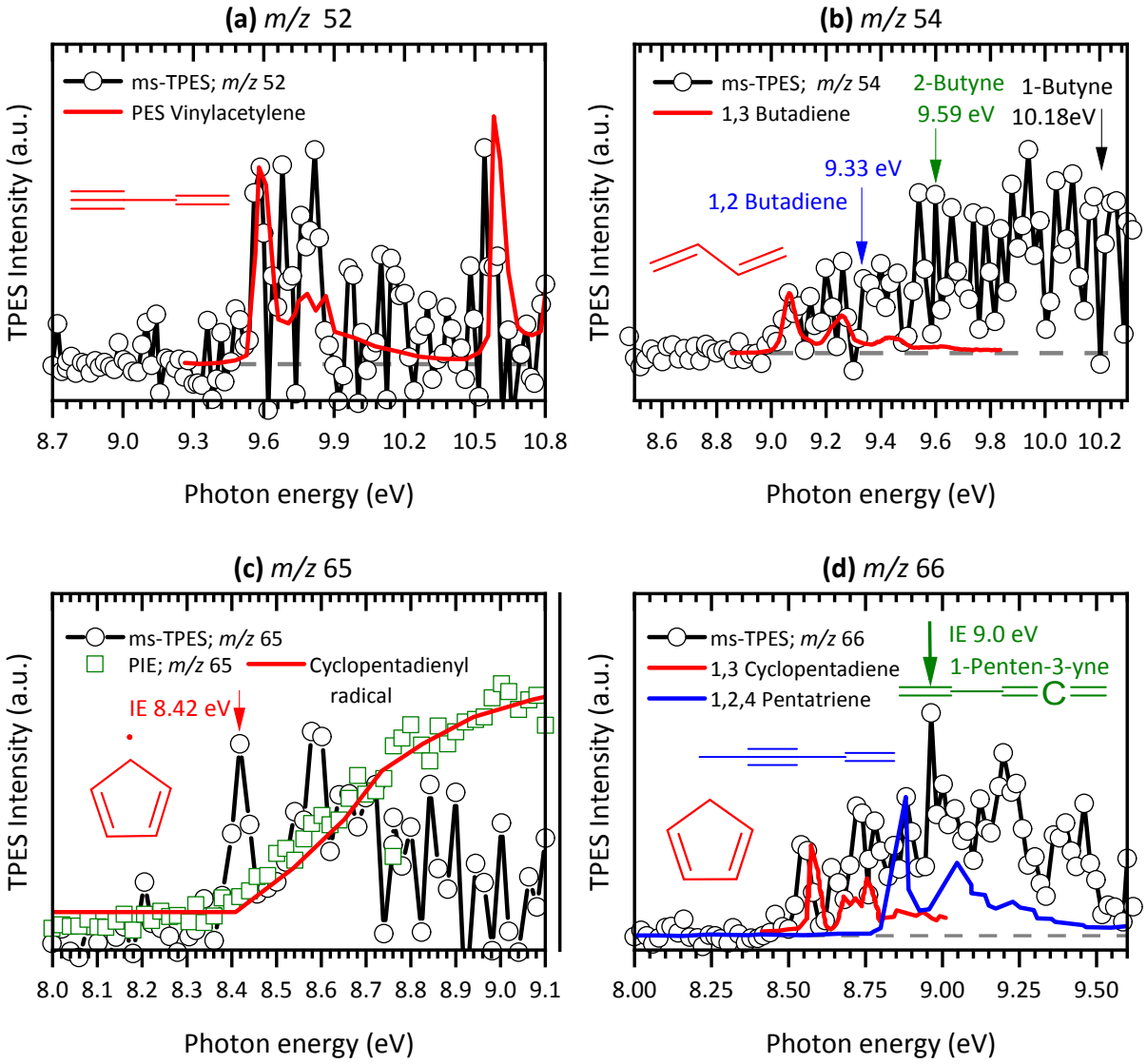

Fig. S 9 Representative examples of product species identification and assignment for C_4-C_5 hydrocarbons and oxygenated species in the pyrolysis of $Al(C_5H_7O_2)_3$ using TPE-spectra **(a,b,c,d)** and PIS **(c)** (black lines, dot symbol); Literature reference spectra (red, blue) and cross sections (red) are as follows: **(a)** *m/z* 52 (C_4H_4)[12] **(b)** *m/z* 54 (C_4H_6)[12,13,17] **(c)** *m/z* 65 (C_5H_5)[14] and **(d)** *m/z* 66 (C_5H_6).[12,16,17]

Additional assignments have been made for C_4-C_5 hydrocarbons revealing that beneath the pyrolysis products vinylacetylene[12] is present (see **Fig. S 9 (a)**). The TPE-spectrum for the *m/z* 54 channel reveals the contribution of at least four isomers of C_4H_6, 1,3-butadiene (IE: 9.07 eV[13]), 1,2 butadiene (IE: 9.33 eV[14]), 2-butyne (IE: 9.59 eV[12]) and 1-butyne (IE: 10.18 eV[14]), which were assigned by their literature values and PES (see **Fig. S 9 (b)**). The cyclopentadienyl has been identified among the pyrolysis products with an ionization onset of 8.42 eV by a literature PIS.[15] At least three species reside on the *m/z* 66 channel, where strong evidence has been found for 1,3-cyclopentadiene[16] and 1,2,4-pentatriene[17] by a comparison to literature TPES. Additionally, at 9.0 eV, evidence in the TPES for 1-penten-3-yne[12] has been found.

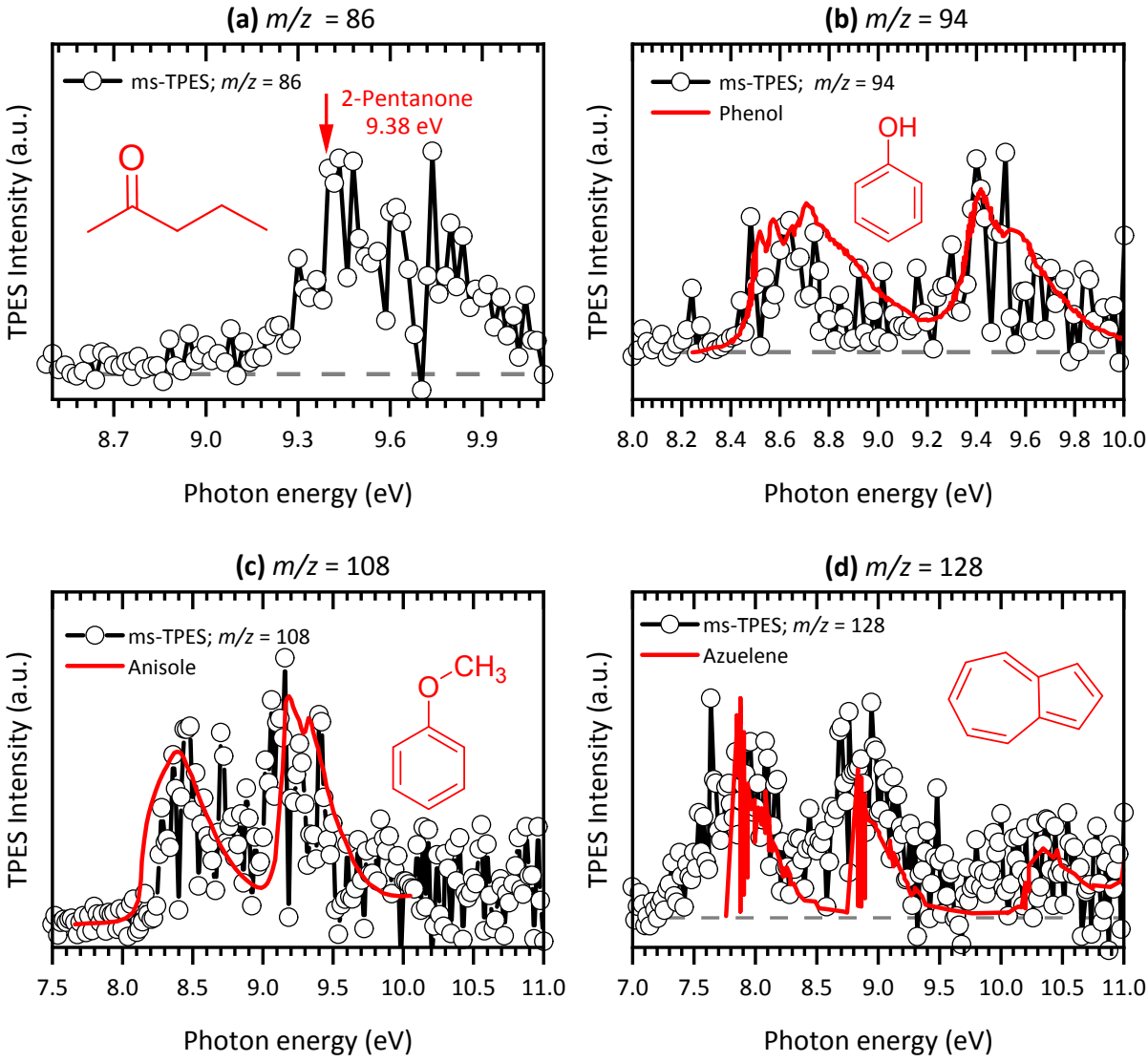

Fig. S 10 Representative examples of product species identification and assignment for C_5-C_{10} hydrocarbons and oxygenated species in the pyrolysis of $Al(C_5H_7O_2)_3$ using TPE-spectra (black lines, dot symbol); Literature reference spectra (red) are as follows: **(a)** *m/z* 86 ($C_5H_{10}O$)[14] **(b)** *m/z* 94 (C_6H_6O)[14] **(c)** *m/z* 108 (C_7H_6O)[18] and **(d)** *m/z* 128 ($C_{10}H_8$).[19]

As far as the C_5-C_{10} hydrocarbons as secondary decomposition products of the pyrolysis of $Al(C_5H_7O_2)_3$ are concerned, we found evidence for 2-pentanone *m/z* 86 ($C_5H_{10}O$)[14], phenol *m/z* 94 (C_6H_6O)[14], anisole *m/z* 108 (C_7H_6O)[18] and azulene *m/z* 128 ($C_{10}H_8$)[19] in the TPE-spectra (see **Fig. S 10**).

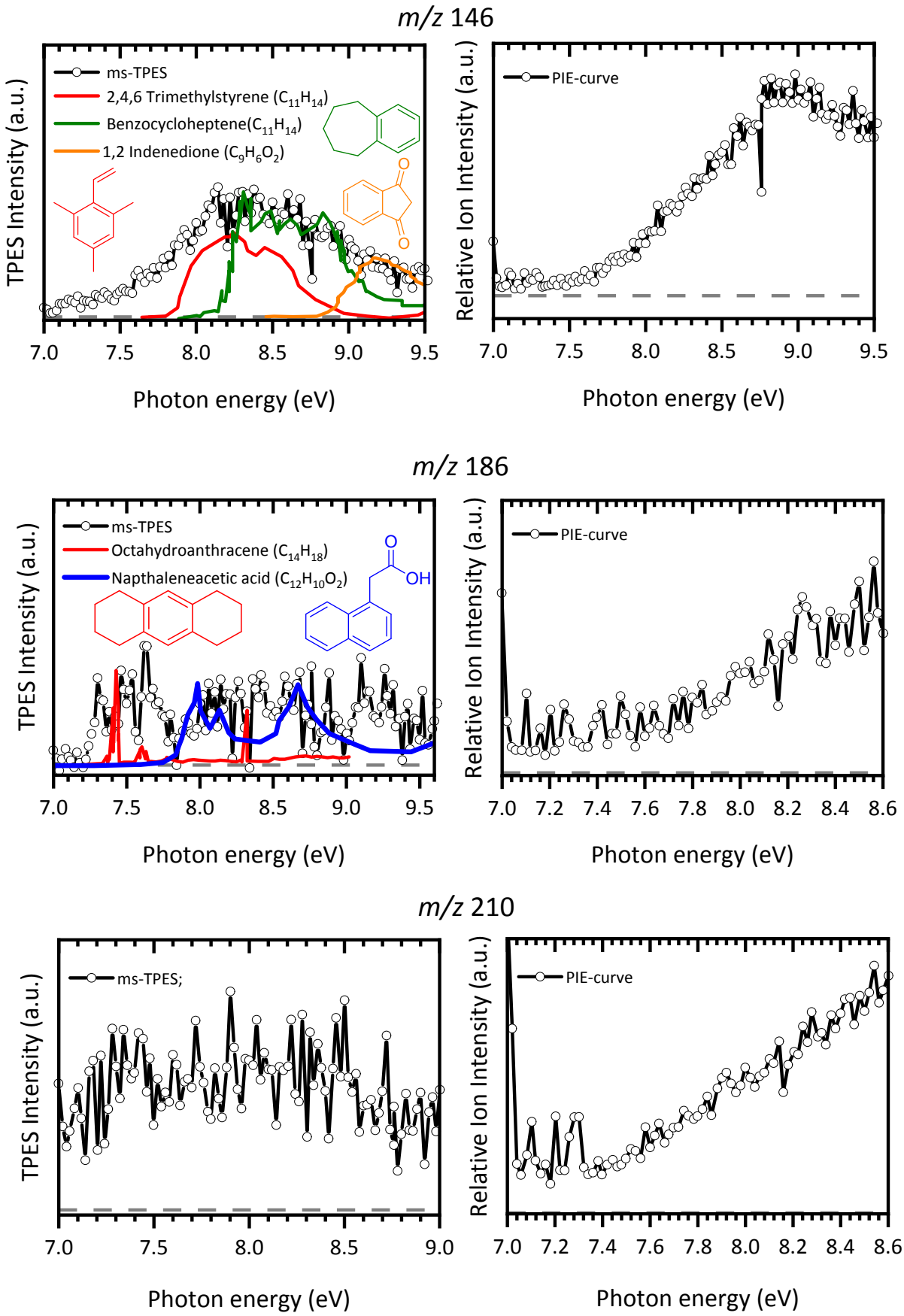

Fig. S 11 Possible product species identification and assignment for *m/z* 146 and 186 formed by pyrolysis of $Al(C_5H_7O_2)_3$ with the aid of ms-TPE-spectra (black lines, dot symbol) as well as ms-TPE-spectra and their respective PIS for *m/z* 146, 186, and 210; Literature reference spectra (red, blue and orange) are as follows: **(top)** *m/z* 146 ($C_{11}H_{14}$; red[20]; green[21]) and ($C_9H_6O_2$; orange[22]); **(middle)** *m/z* 186 ($C_{14}H_{18}$)[18] and ($C_{12}H_{10}O_2$)[18].

S 5 DPI of important pyrolysis products

Fig. S 12 Temperature dependent TPE spectra for *m/z* 100 (left) and *m/z* 43 (right). Important dissociative ionization energies of possible fragments are denoted by green arrows and labelled with their respective parent molecule. The literature reference spectrum is taken from Antonov et al..[23]

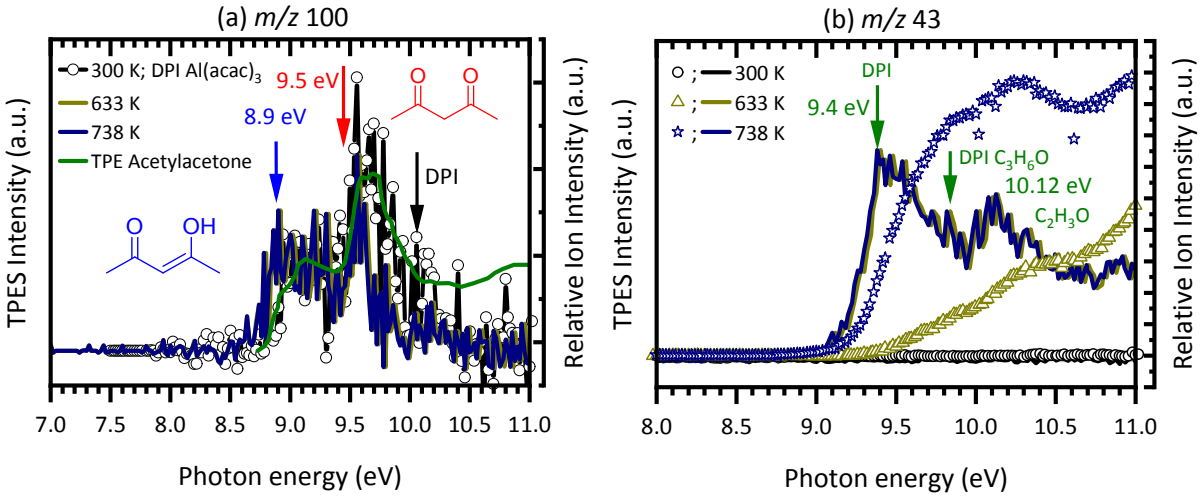

The shape of the TPE-spectra in **Fig. S 12** are in good agreement with the reference spectrum of acetylacetone ($C_5H_8O_2$) in its 97 % enol (IE = 8.9 eV)[23] and 3% diketo (IE: 9.5 eV)[23] tautomers at 300 K. The signal does not follow the reference photoelectron spectrum at photon energies > 10.06 eV, due to DPI, leading to the formation of the major fragments *m/z* 43, 58, 72 and 85.[23] Because of keto-enol tautomerism, gaseous acetylacetone exists primarily in its enol form (first band 8.9 eV) at room temperature, whereas at higher temperatures, the equilibrium shifts to more gaseous diketo-acetylacetone (second band 10.2 eV).[24,23] The central band at 9.5 eV represents a superposition of both tautomer signals. Antonov et al.[23] stated that the *m/z* 43 peak is due to the DPI of diketone-acetylacetone. At temperatures higher than 600 K, the equilibrium constant is around unity,[23] representing similar concentrations of enol- and keto-acetylacetone in the gas phase. This leads to enhanced formation in pyrolysis conditions due to DPI of *m/z* 100.

S6 Influence of surface reactions on the formation of *m/z* 164

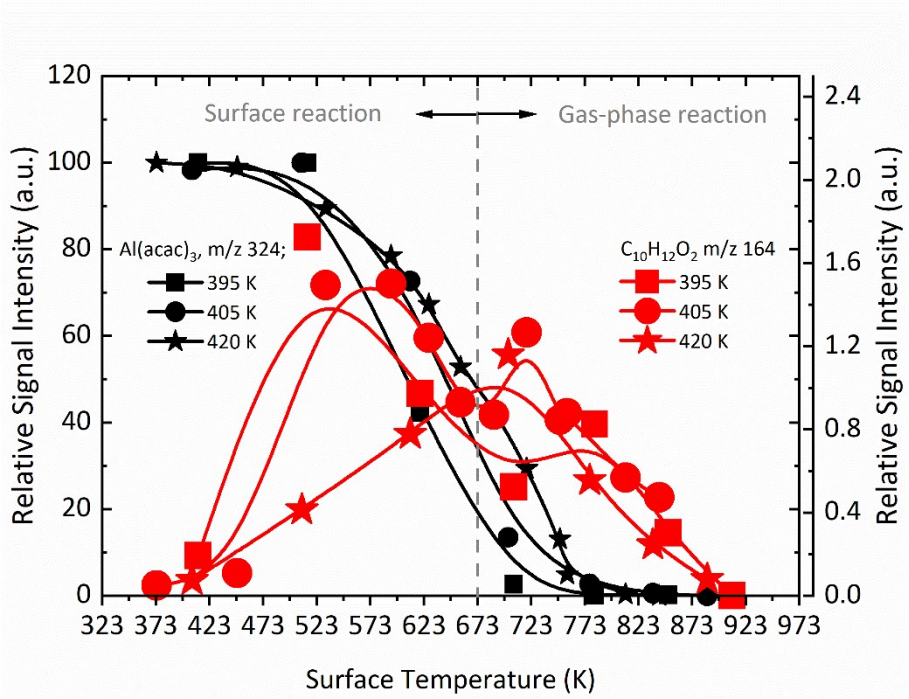

Fig. S 13: Influence of the precursor inlet concentration in form of different evaporation temperatures of 395/ 405 and 420 K on the reaction mechanism leading to the formation of $C_{10}H_{12}O_2$.

According to a review study by Igumenov et al.[25] significant amounts of *m/z* 164 ($C_{10}H_{12}O_2$) may also be formed by heterogeneous surface reactions. Since these reactions are controlled by the $Al(C_5H_7O_2)_3$ feed concentration, we carried out experiments with different evaporation temperatures. A significant difference in the decomposition behavior was observed, supporting the idea that, at low temperatures, surface reactions are dominant in the pyrolysis tube (see **Fig S 13**). The strong increase at 673 K implies that another gas-phase process is also responsible for the formation of *m/z* 164.

References

1. G.A. Bird, *Molecular gas dynamics and the direct simulation of gas flows,* Clarendon Press, Oxford, Oxford science publications, 2003, 42.
2. Morris, Hannon and Garcia, *Phys Rev A*, 1992, **46**(8), 5279.
3. P.J. Weddle, C. Karakaya, H. Zhu, R. Sivaramakrishnan, K. Prozument and R.J. Kee, *Int. J. Chem. Kinet.*, 2018, **50**(7), 473.
4. Q. Guan, K.N. Urness, T.K. Ormond, D.E. David, G. Barney Ellison and J.W. Daily, *International Reviews in Physical Chemistry*, 2014, **33**(4), 447.
5. E.N. Fuller, P.D. Schettler and J.C. Giddings, *Ind. Eng. Chem.*, 1966, **58**(5), 18.
6. M.A. Siddiqi, R.A. Siddiqui and B. Atakan, *Surface and Coatings Technology*, 2007, **201**(22-23), 9055.
7. B.K. Cunha de Miranda, C. Alcaraz, M. Elhanine, B. Noller, P. Hemberger, I. Fischer, G.A. Garcia, H. Soldi-Lose, B. Gans, L.A.V. Mendes, S. Boyé-Péronne, S. Douin, J. Zabka and P. Botschwina, *J Phys Chem A*, 2010, **114**(14), 4818.
8. T.A. Cool, J. Wang, K. Nakajima, C.A. Taatjes and A. Mcllroy, *International Journal of Mass Spectrometry*, 2005, **247**(1-3), 18.
9. B. Niu, D.A. Shirley and Y. Bai, *The Journal of Chemical Physics*, 1993, **98**(6), 4377.
10. G.Y. Matti, O.I. Osman, J.E. Upham, R.J. Suffolk and H.W. Kroto, *Journal of Electron Spectroscopy and Related Phenomena*, 1989, **49**(2), 195.
11. A.J. Yencha, M.R.F. Siggel-King, G.C. King, A.E.R. Malins and M. Eypper, *Journal of Electron Spectroscopy and Related Phenomena*, 2013, **187**, 65.
12. G. Bieri, F. Burger, E. Heilbronner and J.P. Maier, *Helv. Chim. Acta*, 1977, **60**(7), 2213.
13. P. Masclet, G. Mouvier and J.F. Bocquet, *J. Chim. Phys.*, 1981, **78**, 99.
14. Linstrom PJ, Mallard MG, editors, *NIST Chemistry WebBook, NIST Standard Reference Database 69,* Gaithersburg MD, 20899.
15. N. Hansen, S.J. Klippenstein, J.A. Miller, J. Wang, T.A. Cool, M.E. Law, P.R. Westmoreland, T. Kasper and K. Kohse-Höinghaus, *J Phys Chem A*, 2006, **110**(13), 4376.
16. M. Gerlach, A. Bodi and P. Hemberger, *Phys Chem Chem Phys*, 2019, **21**(35), 19480.
17. J. Bouwman, A. Bodi, J. Oomens and P. Hemberger, *Phys Chem Chem Phys*, 2015, **17**(32), 20508.
18. L. Klasinc, B. Kovac and H. Gusten, *Pure and Applied Chemistry*, 1983, **55**(2), 289.
19. H.W. Jochims, H. Rasekh, E. Rühl, H. Baumgärtel and S. Leach, *Chemical Physics*, 1992, **168**(1), 159.
20. T. Kobayashi, K. Yokota and S. Nagakura, *Journal of Electron Spectroscopy and Related Phenomena*, 1973, **2**(5), 449.
21. J.P. Maier and D.W. Turner, *J. Chem. Soc., Faraday Trans. 2*, 1973, **69**(0), 196.
22. V. Galasso, F.P. Colonna and G. Distefano, *Journal of Electron Spectroscopy and Related Phenomena*, 1977, **10**(3), 227.
23. I. Antonov, K. Voronova, M.-W. Chen, B. Sztáray, P. Hemberger, A. Bodi, D.L. Osborn and L. Sheps, *J Phys Chem A*, 2019, **123**(26), 5472.
24. N.S. Hush, M.K. Livett, J.B. Peel and G.D. Willett, *Aust. J. Chem.*, 1987, **40**(3), 599.
25. I.K. Igumenov, A.E. Turgambaeva and P.P. Semyannikov, *J. Phys. IV France*, 2001, **11**(PR3), Pr3-505-Pr3-515.